

AD-A058 719

GEORGIA INST OF TECH ATLANTA

F/8 1/3

RESIDUAL-STRENGTH ANALYSIS OF PRIMARY AIRCRAFT STRUCTURE DAMAGE--ETC(U)

FEB 77 J A ABERSON, J M ANDERSON, W W KING

F08635-76-C-0136

UNCLASSIFIED

61T-E-23-616-VOL-1

AFATL-TR-77-16-VOL-1

NL

| OF |
AD
A058719



AD A058719

AFATL-TR-77-16

LEVEL *11*

Q7

Residual-Strength Analysis of Primary Aircraft Structure Damaged Due to Projectile Impact and Penetration

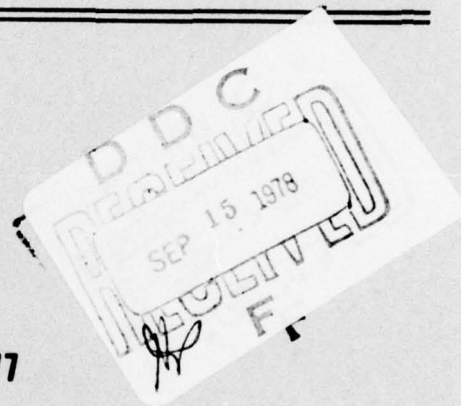
Volume I Test and Analysis

DDC FILE COPY

GEORGIA INSTITUTE OF TECHNOLOGY
ATLANTA, GEORGIA 30332

FEBRUARY 1977

FINAL REPORT FOR PERIOD NOVEMBER 1975 -FEBRUARY 1977



Approved for public release; distribution unlimited



Air Force Armament Laboratory

AIR FORCE SYSTEMS COMMAND • UNITED STATES AIR FORCE • EGLIN AIR FORCE BASE, FLORIDA

78 09 14 014

SECURITY CLASSIFICATION OF THIS PAGE (When Data Entered)

REPORT DOCUMENTATION PAGE		READ INSTRUCTIONS BEFORE COMPLETING FORM	
1. REPORT NUMBER AFATL-TR-77-16, VOLUME I	2. GOVT ACCESSION NO.	3. RECIPIENT'S CATALOG NUMBER	
4. TITLE (and Subtitle) RESIDUAL-STRENGTH ANALYSIS OF PRIMARY AIRCRAFT STRUCTURE DAMAGED DUE TO PROJECTILE IMPACT AND PENETRATION VOLUME I, TEST AND ANALYSIS		5. TYPE OF REPORT & PERIOD COVERED Final Report, November 1975 - to February 1977	
7. AUTHOR(s) J. A. Aberson, J. M. Anderson W. W. King		6. PERFORMING ORG. REPORT NUMBER E-23-616	
9. PERFORMING ORGANIZATION NAME AND ADDRESS Georgia Institute of Technology Atlanta, Georgia 30332		8. CONTRACT OR GRANT NUMBER(s) F08635-76-C-0136	
11. CONTROLLING OFFICE NAME AND ADDRESS Air Force Armament Laboratory Armament Development and Test Center Eglin Air Force Base, Florida 32542		10. PROGRAM ELEMENT, PROJECT, TASK AREA & WORK UNIT NUMBERS Project No. 2549 Task No. 01 Work Unit No. 018	
14. MONITORING AGENCY NAME & ADDRESS (if different from Controlling Office)		12. REPORT DATE February 1977	
		13. NUMBER OF PAGES 57	
		15. SECURITY CLASS. (of this report) UNCLASSIFIED	
16. DISTRIBUTION STATEMENT (of this Report) Approved for public release; distribution unlimited		15a. DECLASSIFICATION/DOWNGRADING SCHEDULE	
17. DISTRIBUTION STATEMENT (of the abstract entered in Block 20, if different from Report) GIT-E-23-616-VOL-1			
18. SUPPLEMENTARY NOTES Available in DDC.			
19. KEY WORDS (Continue on reverse side if necessary and identify by block number) Residual Strength Finite Elements Penetration CRAKD Impact Bending Fracture Stress-Intensity Factors Cracks Computer Code			
20. ABSTRACT (Continue on reverse side if necessary and identify by block number) High-strength aluminum channels, damaged by projectile impacts, have been loaded to failure in pure bending. In cases where damage included cracks of significant lengths, failure loads have been compared with those predicted by linear fracture mechanics through a finite-element computer program (CRAKD) which contains special crack-tip stress-singularity elements. CRAKD has been employed for the computation of time-dependent stress-intensity factors in several problems of elastodynamic fracture. The results demonstrate the importance of specimen inertia in impact tests designed for the			

DD FORM 1 JAN 73 1473

EDITION OF 1 NOV 65 IS OBSOLETE

UNCLASSIFIED

SECURITY CLASSIFICATION OF THIS PAGE (When Data Entered)

153 800

UNCLASSIFIED

SECURITY CLASSIFICATION OF THIS PAGE(When Data Entered)

20. (CONCLUDED) → determination of dynamic fracture toughness. ←

UNCLASSIFIED

SECURITY CLASSIFICATION OF THIS PAGE(When Data Entered)

PREFACE

This report was prepared by the Georgia Institute of Technology, Atlanta, Georgia 30332, under Contract No. F08635-76-C-0136 with the Air Force Armament Laboratory, Armament Development and Test Center, Eglin Air Force Base, Florida 32542. Dr. Kevin T. McArdle (DLYV) managed the program for the Armament Laboratory. This effort was conducted during the period from November 1975 to February 1977.

This report consists of two volumes. Volume I contains the Test and Analysis, and Volume II contains User Guides for the Computer Program. This is Volume I.

This technical report has been reviewed and is approved for publication.

FOR THE COMMANDER:

J. R. Murray
J. R. MURRAY
Chief, Analysis Division

ACCESSION for	
NTIS	White Section <input checked="" type="checkbox"/>
DDC	Buff Section <input type="checkbox"/>
UNANNOUNCED	<input type="checkbox"/>
JUSTIFICATION	
BY	
DISTRIBUTION/AVAILABILITY CODES	
Dist.	SP. CIAL
<i>A</i>	

TABLE OF CONTENTS

Section	Title	Page
I.	INTRODUCTION	1
II.	TEST AND ANALYSIS OF DAMAGED BEAMS	2
	2.1 Residual Strength Determination	2
	2.2 Receipt Schedule of Test Specimens	2
	2.3 Testing Conditions	4
	2.4 Initial Condition and Failure Mode of Specimens	8
	2.5 Stress-Intensity Factors	18
	2.6 Other Damage Sites and Interactions.	25
	2.7 Equivalent Reductions of Section Modulus and Stiffness.	27
III.	COMPARISONS OF MASS DISTRIBUTIONS AND TIME-INTEGRATION ALGORITHMS	29
IV.	FINITE-ELEMENT SIMULATIONS OF IMPACT TESTS	37
	4.1 Introduction	37
	4.2 The Tests of Madison and Irwin	37
	4.3 The Tests of Kobayashi and Chen	45
	4.4 Conclusion	48
V.	CONCLUSIONS	49
	REFERENCES	50

LIST OF FIGURES

Figure	Title	Page
1.	Test Configuration	5
2.	Photographs of Test Configuration	7
3.	Failed Test Section of Specimen 20	10
4.	Failed Test Section of Specimen 22	11
5.	Failed Test Section of Specimen 26	12
6.	Failed Test Section of Specimen 30	14
7.	Failed Test Section of Specimen 109	16
8.	Failed Test Section of Specimen 124	19
9.	Finite-Element Representation of One-Half the Test Section	21
10.	Residual Strength Versus Crack Length	24
11.	Interaction of Nearby Damage Sites	26
12.	Chen's Problem and Its Finite-Element Representation	30
13.	Comparison of Results Obtained Using Finite-Difference and Finite-Element Methods for Chen's Problem.	32
14.	Effect of Inertia Characterization for Chen's Problem	33
15.	Effect of Time-Step Size for Chen's Problem	35
16.	Geometry and Load-Record in the Madison-Irwin Impact Test	40
17.	Finite-Element Model of the Madison-Irwin Specimen	41
18.	Results of Finite-Element Analyses of the Madison- Irwin Impact Test	43
19.	Finite-Element Model of the Kobayashi-Chen Dynamic Tear Test	46
20.	Computed K_1 and Hammer Acceleration for a Dynamic Tear Test	47

LIST OF TABLES

Table	Title	Page
1.	Residual Strengths and Normalized Relative Deflections.	3
2.	Computed Stress-Intensity Factors and Critical Bending Moments	23

SECTION I

INTRODUCTION

The work reported in this document pertains to assessments of residual strengths of damaged aircraft structural elements and to the development of numerical techniques for analysis of elastodynamic problems of cracked bodies.

In Section II are reported the results of loading-to-failure aluminum channels previously damaged by projectile impacts by the Vulnerability Assessments Branch of the Air Force Armament Laboratory. In cases where this damage includes cracks of significant lengths, the experimentally determined failure loads are compared with the predictions of linear elastic fracture mechanics. The theoretical predictions are obtained from a finite-element computer program (CRAKD) utilizing special crack-tip stress-singularity elements for the determination of stress-intensity factors.

A description of the finite-element program, CRAKD, is presented in Volume II. Included are user instructions and sample problems of two-dimensional transient motions of elastic bodies with stationary cracks.

Results of employing different characterizations of inertia (lumped mass and consistent mass) and different time integration algorithms (central difference and Newmark- β) in CRAKD are compared in Section III.

In Section IV finite-element simulations of two impact tests are presented. The significance of specimen inertia in such tests and the problem of extracting dynamic fracture toughnesses from experimental measurements are discussed.

SECTION II

TEST AND ANALYSIS OF DAMAGED BEAMS

2.1 RESIDUAL STRENGTH DETERMINATION

The damaged beams arrived at Georgia Institute of Technology in quantities and on dates given in paragraph 2.2. They were tested under conditions described in paragraph 2.3. Briefly, the beams were loaded in a manner corresponding to pure bending in an 18-inch longitudinal test section containing the damage. The load was increased until the test section failed. The failure moment in the test section was taken to be the residual strength of the damaged beam. The normalized relative deflection of the center and edge of the test section was measured for selected beams thought to be characteristically damaged. The residual strengths and normalized relative deflections are found in Table 1.

2.2 RECEIPT SCHEDULE OF TEST SPECIMENS

One undamaged beam carrying no numerical designation arrived at the Georgia Institute of Technology on 19 December 1975. It was boxed and well protected from the environment. This beam was originally felt necessary to the program to provide a baseline from which to judge subsequently supplied damaged beams. However, some of the later beams were so lightly scarred that the function of the undamaged beam now seems unnecessary. It has not been tested to date.

The first shipment of damaged beams arrived at Georgia Institute of Technology on 27 February 1976. The shipment consisted of twelve beams (specimen numbers 17 to 32 in Table 1) strapped to a skid. Although exposed

TABLE 1. RESIDUAL STRENGTHS AND NORMALIZED RELATIVE DEFLECTIONS

SPECIMEN NUMBER	RESIDUAL STRENGTH (in-kips)	NORMALIZED RELATIVE DEFLECTION ($\frac{1000 \times \text{in}}{\text{in-kips}}$)
17	70.5	8.67
19	47.3	6.93
20	93.0	8.00
21	105.0	4.80
22	262.5	2.33
25	600.0	1.33
26	495.0	4.40
27	472.5	4.00
28	510.0	3.07
30	26.3	
31	457.5	2.53
32	240.0	2.00
61	57.8	9.33
62	417.8	
65	487.5	
66	501.0	
69	451.5	
94	435.0	
98	21.8	14.67
109	487.5	
110	510.0	
111	354.0	
112	414.0	
114	507.8	
115	335.3	
116	309.8	
117	331.5	
118	513.8	
119	315.0	
120	396.0	
122	415.5	
124	513.0	
125	424.5	

to the environment, the beams did not seem to have suffered any substantial deterioration.

The last shipment of damaged beams arrived at Georgia Institute of Technology on 8 June 1976. It consisted of 21 individually boxed beams (specimen numbers 61 to 125 in Table 1).

2.3 TESTING CONDITIONS

The damaged beams were tested to failure in the Structures Laboratory of the Civil Engineering School at Georgia Institute of Technology. The test machine involved was a RIEHLE screw-type of 450-kip capacity. It was last calibrated by Southern Calibration and Service of Atlanta, Georgia 30326, on 6 January 1976. The maximum load registered during the test program was 80 kips, and failure loads were read to the nearest 100 pounds. A constant loading rate (descent) of 0.2 inch per minute was used throughout the test program.

The four-point-bending configuration is shown in Figure 1. A long steel support beam (12 WF 36) was placed on the base of the test machine. Two vertical supports approximately 12 inches high and tapering to 1-3/8-inch diameter steel roller supports were positioned on the support beam 3 inches inside each end of the 5-foot specimen. A 21-inch section on each end of the specimen was enclosed in a steel support box to prevent rotation of the specimen's unsymmetrical cross-section about a longitudinal axis. Steel loading rollers (1-3/8-inch diameter) were placed 3 inches from the inner end of each steel support box giving an effective 15-inch shear section on each end of the specimen. The loading rollers were held in place by a 6-foot

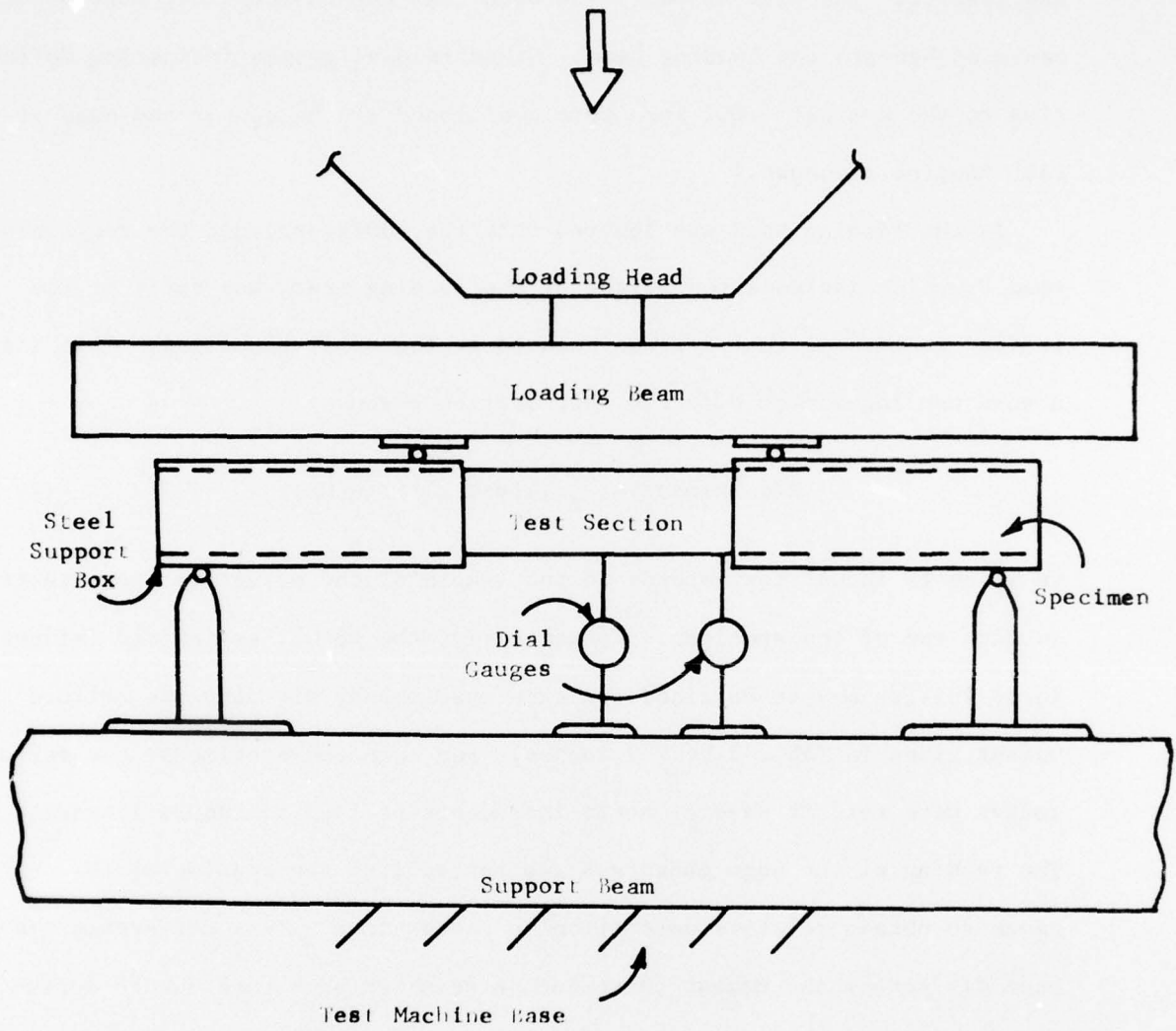


Figure 1. Test Configuration

steel loading beam (6 WF 25) onto which the loading head of the test machine was lowered. The test assembly was such that the 18-inch test section was centered beneath the loading head. Standard dial gauges indicating deflection to the nearest 0.001 inch were positioned at the center and edge of the test section as shown.

As the loading head was lowered onto the configuration, the registered load P , which includes the weight of the loading beam, was split at the loading rollers so that $P/2$ was reacted at the support rollers. This induced a pure bending moment M in the test section given by

$$M(\text{in-kips}) = \frac{P}{2} (\text{kips}) \times 15(\text{inches}) , \quad (1)$$

in which 15 inches corresponds to the length of the effective shear section on each end of the specimen. Consequently, the actual registered failure loads in kips may be obtained for each specimen by dividing the failure moment given in Table 1 by 7.5 inches. For selected specimens, the deflection gauges were read at several early increments of load to insure linearity. The reading of the edge gauge was subtracted from the reading of the center gauge to obtain relative deflection in thousandths. This difference was then divided by the moment increment between two such readings to arrive at the compliances indicated in Table 1. The gauges were then removed, and the specimen was loaded to failure at the previously indicated rate. All specimens failed in the test section.

Six photographs are included in this paragraph to aid in describing the test configuration. Figure 2(a) shows a view taken from the front and to the right of the test assembly. The specimen shown in this and subsequent

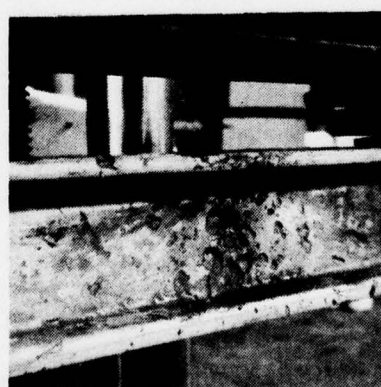
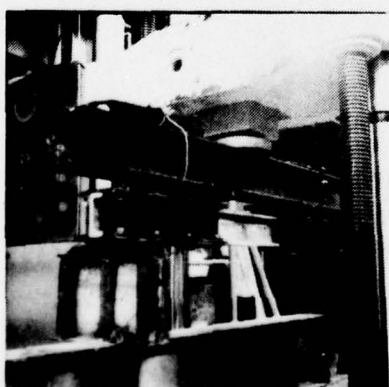
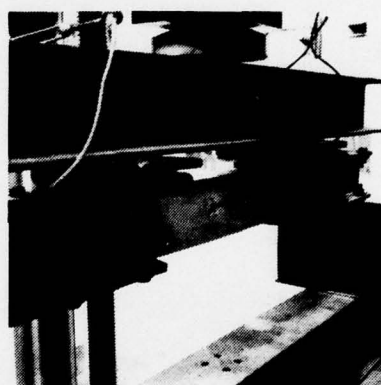
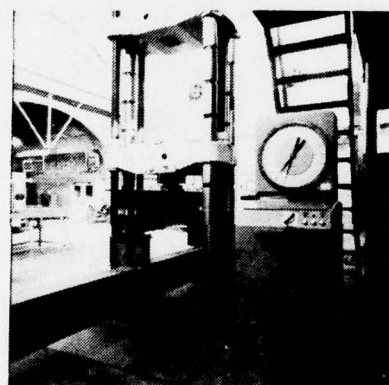
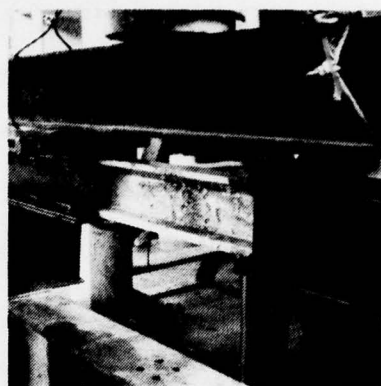
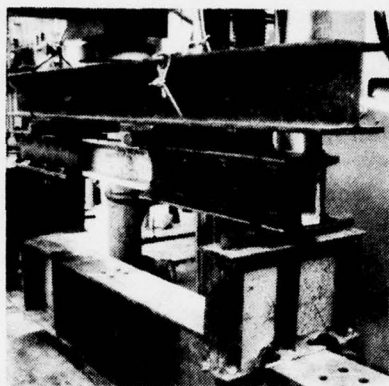


Figure 2. Photographs of Test Configuration

photographs is number 118; the deflection gauges are not shown because compliance measurements were not taken for this specimen. The cable looped around the loading beam was used to prevent it from falling when the specimen failed. The support boxes are shown most clearly in Figure 2(a).

Basically they were each made of two 21-inch sections of 5 x 9 steel channel with 5/16-inch-thick steel cover plates fastened by sixteen 1/2-inch-diameter by 2-inch-long A325 heavy hex bolts and nuts. Figure 2(b) shows a closer view taken at the same angle and begins to reveal a heavily scarred web in the test section of specimen 118. Figure 2(c) shows a view of the test machine and console taken from behind and to the left of the test assembly. A closer view taken at the same angles is shown in Figure 2(d) where some spalling at the outer web surface is evident. Figures 2(e) and 2(f) show two views taken from the front and to the left of the test assembly. Details of the damage inflicted on the inner web surface of the test section are most evident in Figure 2(f).

2.4 INITIAL CONDITION AND FAILURE MODE OF SPECIMENS

Specimen 17 was heavily scarred in both flanges and the web. Failure progressed from a 1-1/8x9/16x13/32-inch deep gouge at the tip of the through-cracked lower flange up along web scars and finished at a gouge in the tip of the upper flange. The crack arrested several times in the web. The initial crack length was just over the flange thickness of 5/8 inch.

Specimen 19 had a 1 1/2-inch-long initial crack extending through the lower flange and into the web where it had turned in the longitudinal direction. The crack arrested several times in the web before exiting at a gouge in the tip of the upper flange. The crack arrested several times in the web. The initial crack length was just over the flange thickness of 5/8 inch.

Specimen 19 had a 1 1/2-inch-long initial crack extending through the lower flange and into the web where it had turned in the longitudinal direction.

in the upper flange.

Specimen 20 had the same type initial crack as specimen 19 except that it was only 7/8-inch long, i.e., just through the lower flange and 1/4-inch into the web. Figure 3 shows the failed test section of this specimen. The lower flange is shown on top to more clearly reveal the initial fracture surface which appears very dark in the photograph. The web was only moderately scarred, and the crack did not seem to select a path of greatest damage as it propagated through the section, exiting at one of the smaller gouges in the upper flange.

Specimen 21 also had a 7/8-inch-long initial crack through the lower flange and into the web. It failed in almost exactly the same manner as specimen 20 except that the crack arrested about three-fourths of the way through the web at one of the heavier scars on the web.

Specimen 22 had no visible initial crack, but the lower flange (shown on top in Figure 4) had a 45/64-inch-long by 21/64-inch-deep gouge at its tip. The failure initiated at this gouge and resulted in sudden fracture of the entire section.

Specimen 25 had a 1-inch diameter central hole in the web but no damage to the lower flange. The loading beam contacted the ends of the support boxes in the test of this specimen, which finally failed by torsional buckling of the test section. The buckling produced longitudinal cracks emanating from the hole in the web and a longitudinal crack in the upper flange originating at a deep gouge.

Specimen 26 had a clean lower-flange outer surface as shown on top in Figure 5. The inner surface of the lower flange and web were moderately

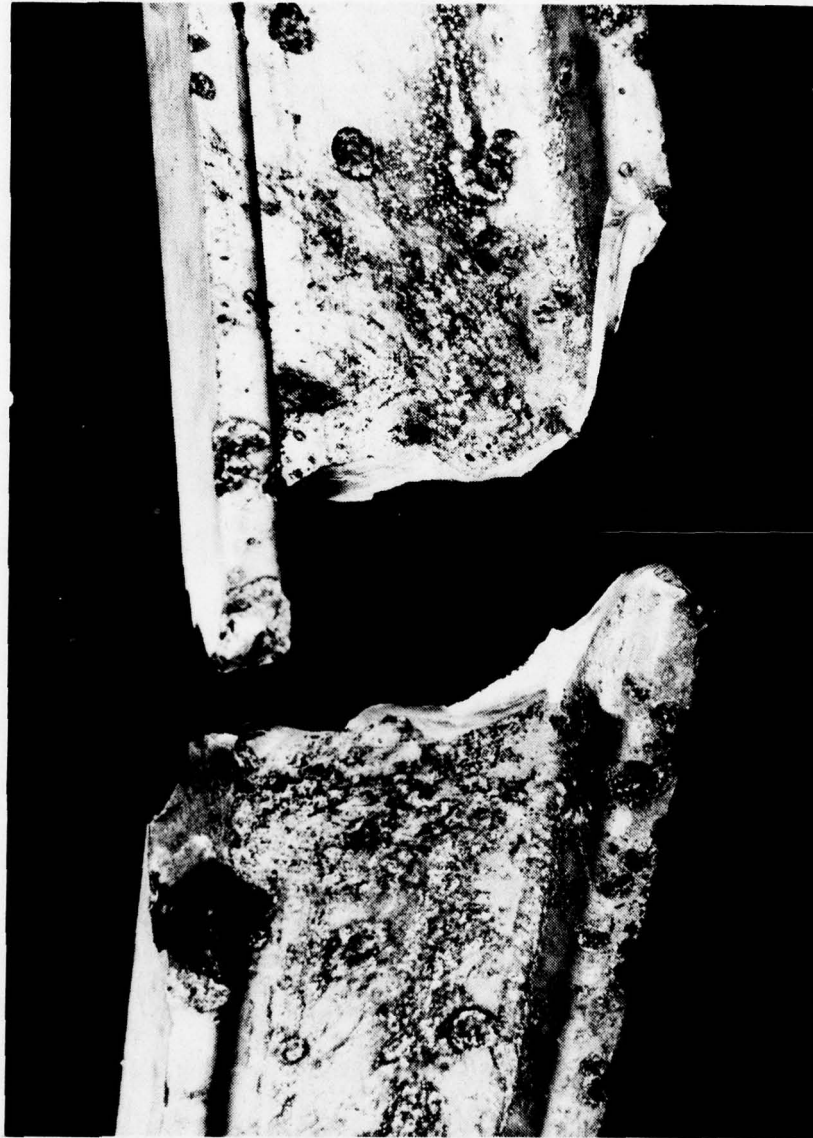


Figure 3. Failed Test Section of Specimen 20



Figure 4. Failed Test Section of Specimen 22



Figure 5. Failed Test Section of Specimen 26

scarred. The section failed suddenly with the fracture branching about halfway through the web.

Specimen 27 also had a clean lower-flange outer surface, but the tip had several light gouges. One of these gouges was 1/4-inch deep, but the fracture originated at a shallower (7/64-inch) gouge which more nearly involved the entire flange thickness. The failure load was practically the same as that for specimen 26, but there was no crack branching.

Specimen 28 had virtually no damage to the lower flange, and the web was only lightly scarred. This specimen failed by torsional buckling in the test section which propagated a longitudinal fracture at the web-upper flange intersection.

Specimen 30 is shown in Figure 6. It had an irregularly shaped hole in the web with some peripheral fracture surface parallel to the plane of the web. The upper flange was through cracked with the crack extending into the hole. Unfortunately this beam was tested upside down and consequently showed practically no residual strength.

Specimen 31 had its fracture originate from a practically hemispherical (13/32x21/64x12/32-inch) gouge in the inner surface of the lower flange.

Specimen 32 was heavily scarred overall but uncracked. Fracture originated at a 1/2-inch-deep gouge at the tip of the lower flange and involving its entire thickness. This deep gouge was connected to a shallower (13/64-inch) gouge at the inner surface of the lower flange.

Specimen 61 had a 1 1/4-inch initial crack through the lower flange and into the web.

Specimen 62 had no visible initial crack. Fracture originated at a



Figure 6. Failed Test Section of Specimen 30

deep gouge at the tip of the lower flange. The precise dimensions of the gouge cannot be determined as a small piece of the lower flange broke off as the beam failed and was never recovered.

Specimen 65 had no visible initial crack. Fracture originated at a nearly circular ($11/32 \times 12/32$ -inch) gouge at the tip of the lower flange that was $15/64$ -inch deep.

Specimen 66 had no visible initial crack. Fracture originated at a $3/16$ -inch deep gouge at the tip of the lower flange. The longitudinal and vertical dimensions of the gouge were $19/64$ inch and $15/64$ inch, respectively.

Specimen 69 had no visible initial crack. Fracture originated at a practically hemispherical ($15/64 \times 1/4 \times 1/4$ -inch) gouge at the tip of the lower flange. A bigger ($1/2 \times 27/64 \times 13/32$ -inch) gouge in essentially the same location did not promote fracture.

Specimen 94 had no visible initial crack. Fracture originated at a gouge in the tip of the lower flange measuring $27/64$ -inch long by $21/64$ -inch high by $17/64$ -inch deep.

Specimen 98 had a $2-1/2$ -inch initial crack through the lower flange and halfway through the web. This specimen provided the least residual strength of all those tested.

Specimen 109 is typical of most of the specimens with no initial crack. It is shown in Figure 7 with the lower flange on top. Fracture originated at a $15/64 \times 9/64 \times 15/64$ -inch gouge at the inner corner of the tip of the lower flange. The dark part of the lower flange fracture surface in Figure 7 is grease that got on the specimen as it fell onto the support beam. Notice



Figure 7. Failed Test Section of Specimen 109

that the propagating crack branched again in this specimen nearly resulting in a three-piece fracture with the smallest piece almost exactly the same shape as the one shown in Figure 5.

Specimen 110 had no visible initial crack. Fracture originated at the inner surface of the lower flange from a $3/32$ -inch deep, nearly circular ($7/16 \times 13/32$ -inch) gouge.

Specimen 111 had no visible initial crack but had a gouge at the tip of the lower flange that involved the full thickness and measured $3/8$ -inch deep at the outer surface of the lower flange.

Specimen 112 failed from a gouge at the inner corner of the tip of the lower flange acting in combination with a separate but nearby gouge at the outer corner of the tip of the lower flange. The first gouge was about $3/8$ -inch deep at its deepest part while the second gouge was only about $1/4$ -inch deep.

Specimen 114 had no visible initial crack. It failed from a $1/4$ -inch deep gouge at the outer corner of the tip of the lower flange.

Specimen 115 had no visible initial crack but had a gouge at the tip of the lower flange involving the full thickness and measuring just over $1/2$ -inch deep at its deepest part.

Specimen 116 had damage of almost exactly the same severity and location as specimen 115.

Specimen 117 had connected inner corner and outer corner gouges of about $1/4$ -inch depth.

Specimen 118 had no visible initial crack. Fracture originated at a triangular-shaped gouge on the inner surface of the lower flange. The legs of the triangle were about $1/2$ -inch long, and the gouge was $9/64$ -inch

deep. The fracture bifurcated near the intersection of the web and upper flange, resulting in a three-piece failure. The fracture surface bypassed a small nearby hole in the web.

Specimen 119 had damage of almost exactly the same severity and location as specimen 115.

Specimen 120 had a small gouge at the inner corner of the lower surface. The fracture bifurcated and almost resulted in a three-piece failure (see Figure 7).

Specimen 122 was sparsely though deeply gouged in the web and upper flange. There were no visible initial cracks, and the fracture originated at a shallow ($7/32$ -inch) gouge at the tip of the lower flange.

Specimen 124 is shown in Figure 8 with the lower flange up to show more clearly the nick at the outside corner that promoted fracture. The dark grease spot on the lower flange should again be ignored as it was picked up as the broken beam impacted the support beam.

Specimen 125 had no visible initial cracks. Fracture originated at a substantial ($9/16$ -inch long by $13/32$ -inch high by $11/32$ -inch deep) gouge at the outer corner of the lower flange.

2.5 STRESS INTENSITY FACTORS

With the exception of the two specimens which failed due to torsional buckling of the test section (numbers 25 and 28), the failure mode was generally one of crack propagation from the lower flange vertically upward through the remainder of the section. Consequently, it was felt that a finite-element representation of one-half the test section (i.e., taking

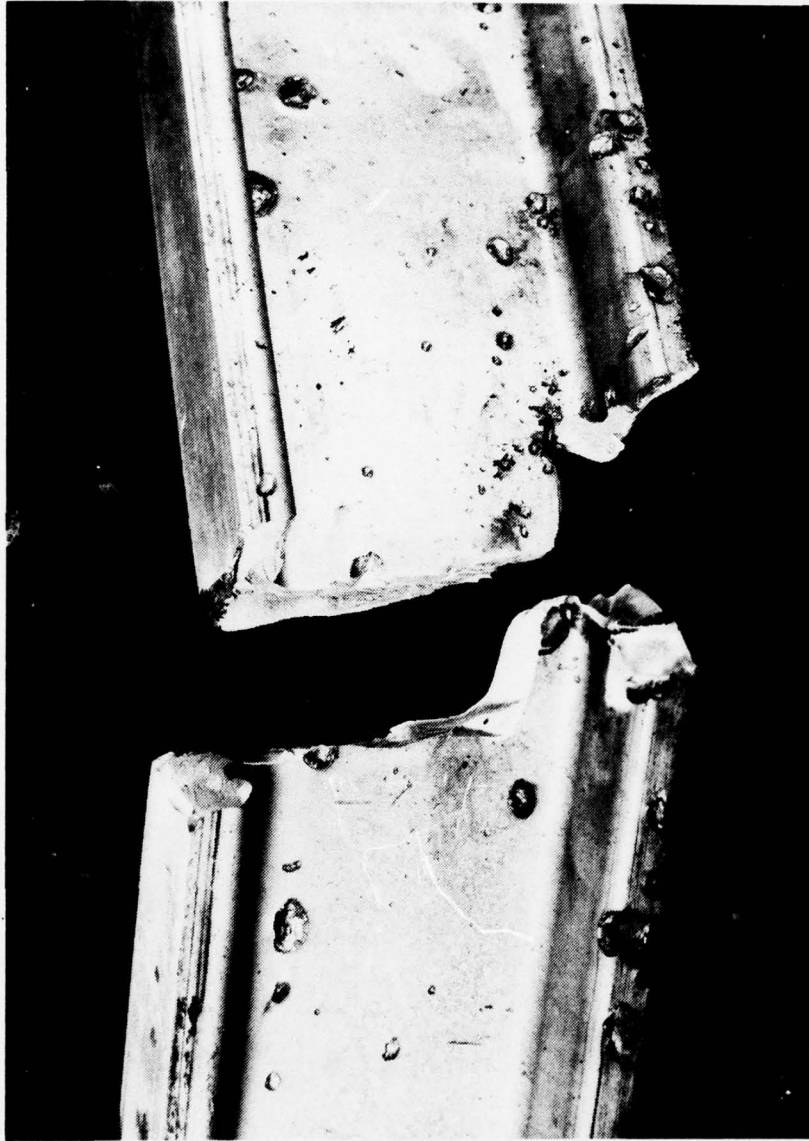


Figure 8. Failed Test Section of Specimen 124

advantage of longitudinal symmetry about a hypothetical, centrally located, plane fracture surface) was appropriate. Figure 9 shows such a finite-element representation.

The finite-element model shown consists of 297 nodes and 514 constant-strain triangles. Nodes along left edge AB correspond to points lying on the crack face and along the prospective fracture surface. Nodes on the crack face are unrestrained; nodes on AB ahead of the crack tip are constrained to move vertically by horizontal forces. All nodes on AB are free of vertical forces, a condition consistent with AB being a line of symmetry. Free edges BC and AD correspond to the outer surfaces of the upper and lower flanges, respectively. Edge CD corresponds to the right-hand end of the test section. Nodes on this edge were subjected to horizontal forces whose distribution vertically is statically equivalent to the classical continuous stress distribution resulting from a unit in-kip applied bending moment.

The thickness of the flanges (represented by the upper and lower horizontal bay of triangles in the coarser part of the model) was taken to be uniformly equal to 2 inches. The thickness of the web was taken to be uniformly equal to 1/2 inch. Material parameters input were: Young's modulus (E) = 10.3×10^3 ksi; Poisson's ratio (ν) = 0.30. The model shows the 8-node cracked element at A corresponding to the shortest crack length ($a = 3/16$ inch) considered.

The computer program CRAKD was executed for this model first with no initial crack to verify that stresses due to the pure bending moment were being adequately computed in the refined section. Theoretically, the maximum bending stresses for a unit in-kip moment and a section modulus of 5.7 in.³

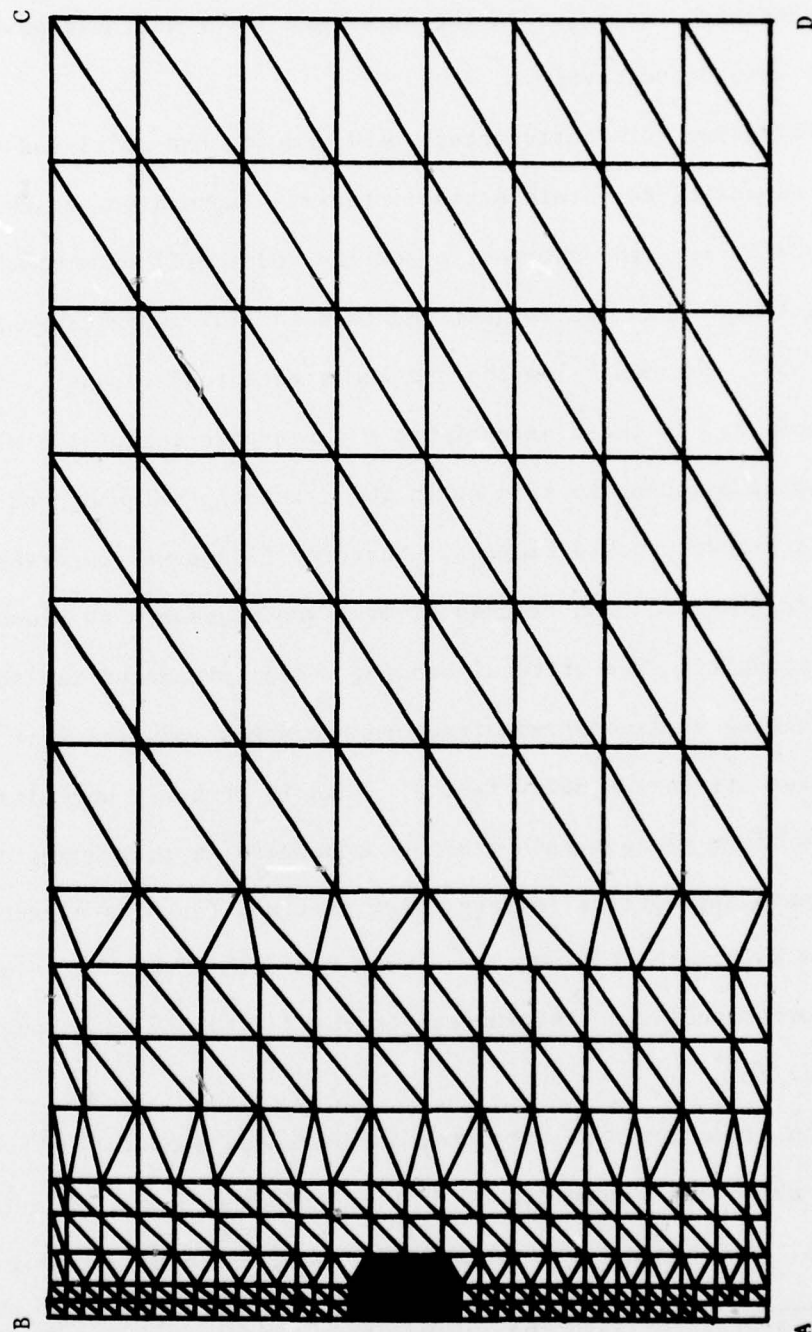


Figure 9. Finite-Element Representation of One-Half the Test Section

($14.24 \text{ in}^4 / 2.5 \text{ in.}$) should be 0.176 ksi. Averages of the two smallest and outermost triangles on the upper and lower surfaces gave -0.174 ksi and 0.175 ksi, respectively.

Following this satisfactory performance, the model and computer program were exploited to obtain stress-intensity factors for crack lengths ranging from 3/16 inch (the shortest crack the model will accommodate) to 2-11/16 inches (just longer than the longest recorded initial crack length in the test program). The crack lengths and computed stress-intensity factors are given in Table 2. In these executions, a three-pair set of the six smallest triangles adjacent to side AB in the crack-tip neighborhood were replaced by the 8-node cracked element. Near the flange-web intersection, overlaying of triangles with the cracked element was necessary to provide the thickness discontinuity. The critical bending moment presented in Table 2 was obtained by dividing a plane-strain fracture toughness value of $26.4 \text{ ksi-}\sqrt{\text{in}}^*$ by the computed stress-intensity factor. This is probably unrealistically conservative since plane-strain fracture toughness is that asymptotic value of toughness appropriate to very thick sections (such as a part-through crack in the 2-inch-thick flange). A more reasonable value of toughness would one corresponding to thicknesses in the 1/2- to 5/8-inch range, i.e., about $50 \text{ ksi-}\sqrt{\text{in}}^{**}$.

The effect of this parameter is presented graphically in Figure 10, which shows the dependence of critical bending moment upon initial crack length. The solid curve is based on the plane-strain fracture toughness

* The average of five room-temperature bend tests of 7075-T6510 extrusions (L-T) given in the Damage Tolerant Design Handbook distributed by the Metals & Ceramics Information Center (HB-01) at Batelle Columbus Laboratories (December 1972).

** Elementary Engineering Fracture Mechanics, by David Broek, published by Noordhoff International Publishing Company in 1974, pp. 184.

TABLE 2. COMPUTED STRESS-INTENSITY FACTORS AND CRITICAL BENDING MOMENTS

CRACK LENGTH (in.)	STRESS-INTENSITY FACTOR ($\text{ksi}\sqrt{\text{in}}$)	CRITICAL BENDING MOMENT (in-kips)
3/16	0.158	167
5/16	0.218	121
7/16	0.284	93
9/16	0.445	59
11/16	0.773	34
13/16	0.771	34
1 3/16	0.842	31
1 9/16	0.968	27
1 15/16	1.146	23
2 5/16	1.379	19
2 11/16	1.715	15

while the dashed curve is based on a toughness of $50 \text{ ksi}\sqrt{\text{in}}$. The specimens which had identifiable initial crack lengths appear in Figure 10 as dots with corresponding specimen numbers. The data appears to agree better with the dotted curve. It is not unexpected that even the cracked specimens by and large exhibit more strength than predicted by routine application of linear fracture mechanics. Firstly, the toughness values used correspond to crack tips sharpened by the application of many low-amplitude fatigue cycles; the specimens were impact cracked and doubtlessly have more blunt crack tips. Secondly, the crack in each specimen, though generally perpendicular to the beam axis, is not always exactly aligned to produce the minimum breaking load for the particular crack length.

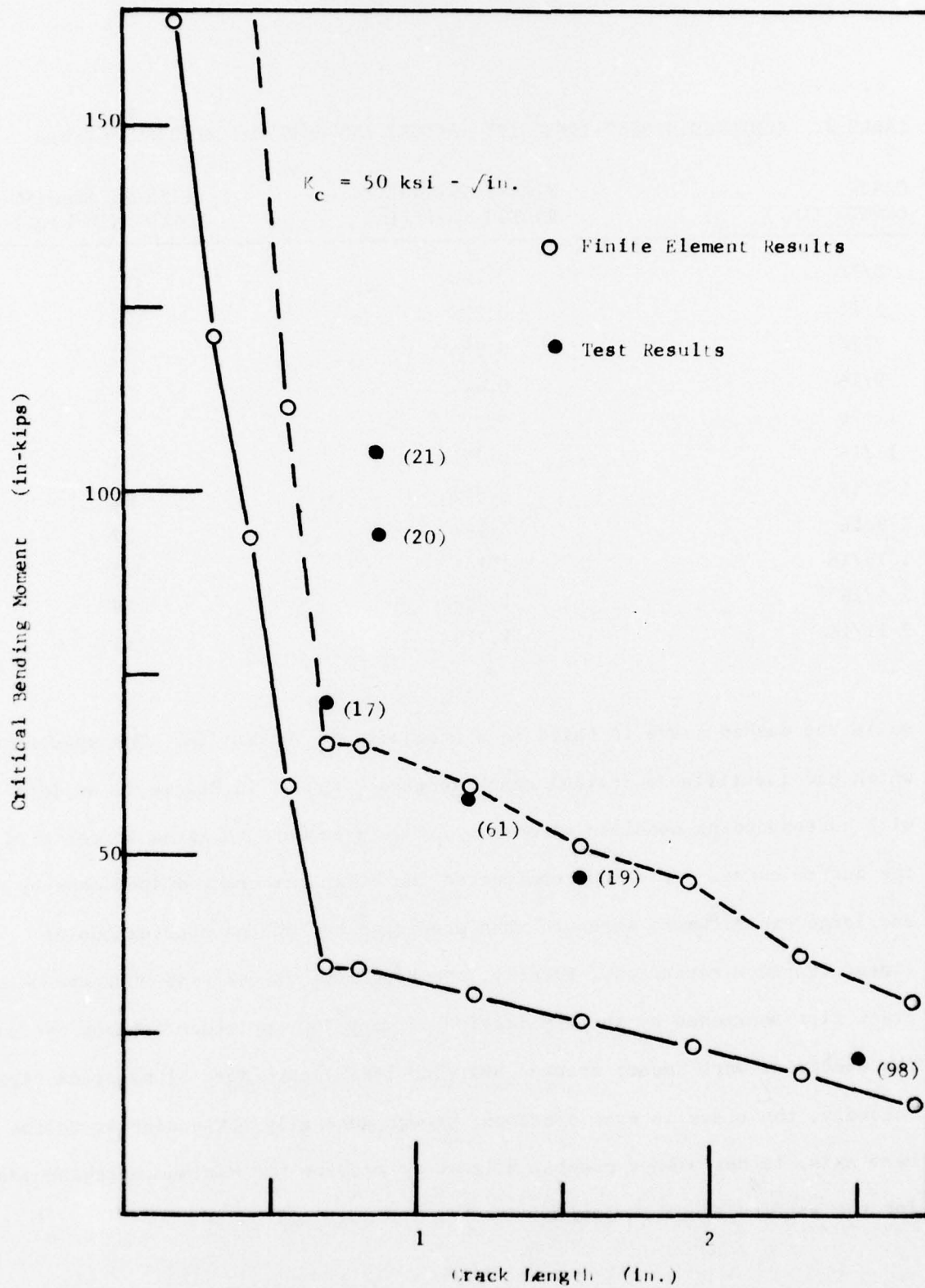


Figure 10. Residual Strength Versus Crack Length

2.6 OTHER DAMAGE SITES AND INTERACTIONS

Based on an inspection of the specimens and an analysis of the test results, there are two alternative locations of through-the-thickness damage, and neither seems to be deleterious to overall strength. A through-cracked upper flange has no effect on residual strength since the fracture surfaces bear on one another in compression. Consequently, unless a load reversal is expected (maneuver, landing, etc.), cracks in the upper flange may be discounted as damage. Several specimens supplied had holes through the web. Despite the considerable visual impression a perforated web makes upon an observer, such damage produces a largely negligible reduction in strength. This was demonstrated very graphically by the test of specimen 25 which had a hole in the web, but whose essentially undamaged flanges sustained sufficient bending moment to promote torsional buckling. Additional evidence to this effect was provided by specimen 118, in which a small hole in the web was bypassed by the propagating fracture surface.

In order to numerically confirm that two damage sites must be almost contiguous to reinforce one another, the finite-element model shown in Figure 9 was modified slightly to produce a central web perforation that measured 1-inch long by $3/4$ -inch high. One-half the perforation is shown shaded in Figure 9. The model was then executed for four crack lengths ($3/16$, $13/16$, $1\ 7/16$, and $2\ 1/16$ inches) measured from the outer surface of the lower flange. Notice that for the longest crack length considered, the crack tip was only $3/16$ inch from the edge of the hole. The results presented as stress-intensity factors (as computed with and without the hole) as a function of crack length are shown in Figure 11. As expected from a recollection of

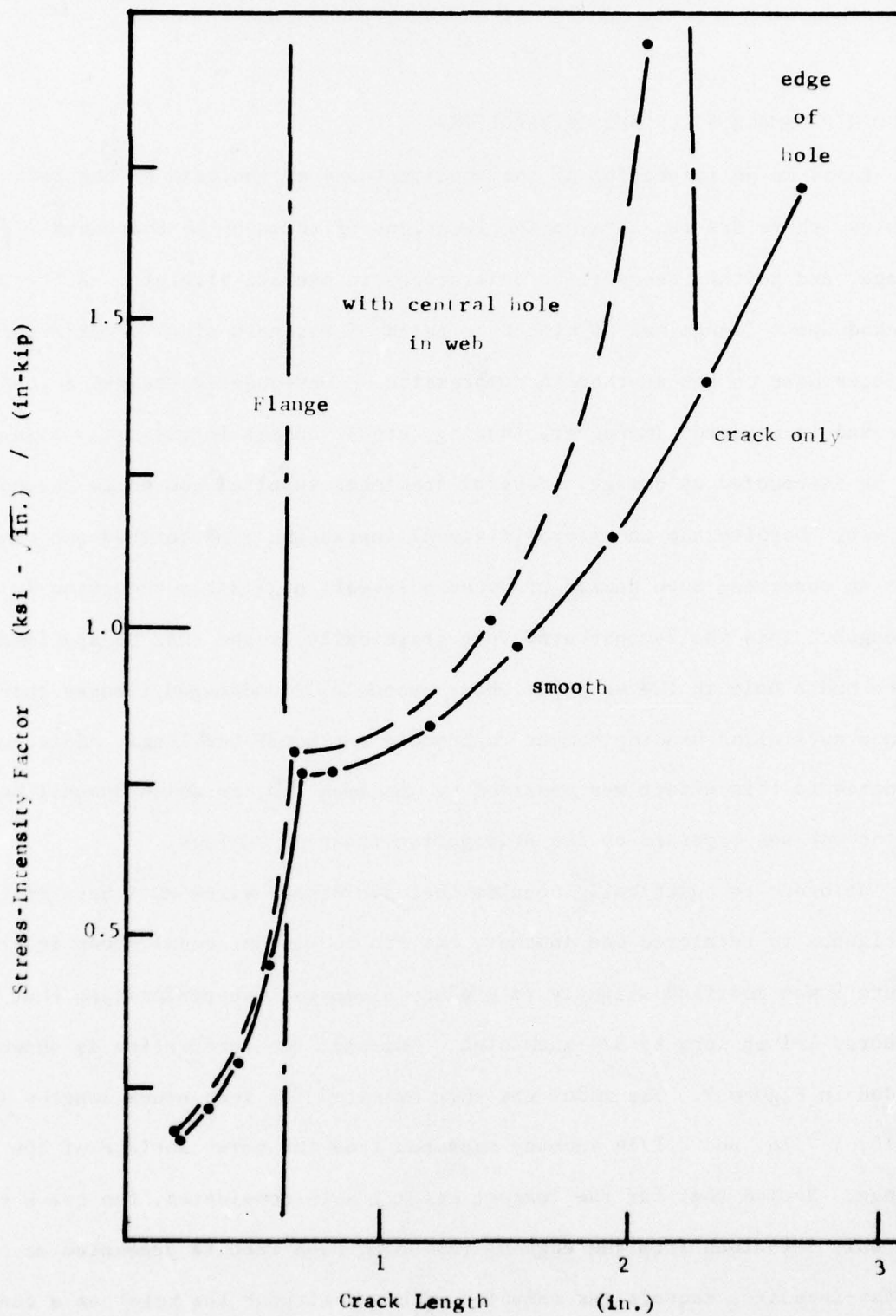


Figure 11. Interaction of Nearby Damage Sites

the test results, the stress-intensity factor is effectively insensitive to the presence of the hole until it is within 1 inch of the edge. Consequently, it is felt that damage interaction can be reasonably ignored in future analyses.

2.7 EQUIVALENT REDUCTIONS OF SECTION MODULUS AND STIFFNESS

The experimental results tend to fall into three groups. The group in which a specimen falls depends primarily on the integrity of its lower flange.

GROUP 1 (MINIMAL DAMAGE TO LOWER FLANGE)

Specimens falling in this group are 26, 27, 31, 62, 65, 66, 69, 94, 109, 110, 112, 114, 118, 120, 122, 124, and 125. The residual strengths of these specimens range from 396-514 (in-kips). A typical compliance is 1.33 (1000 in./in-kips). Damage for this group consists of 1/4-inch (or less) deep gouges involving the full 5/8-inch thickness of the lower flange. Deeper gouges involving less than the full thickness are found in this group. There were no visible initial cracks in this group. No reductions are suggested since the upper end of this strength range corresponds to the onset of torsional buckling.

GROUP 2 (MODERATE DAMAGE TO LOWER FLANGE)

Specimens 22, 32, 111, 115, 116, 117, and 119 fall in this group. Residual strengths are in the 240-354 (in-kip) range. A typical compliance is 2.4 (1000 in./in-kips). Damage for this group characteristically consists of through-the-thickness gouges deeper than 1/4 inch. There were no visible cracks in this group. A uniform section modulus and stiffness reduction of 40 percent from values for nominally undamaged specimens is suggested for this group.

GROUP 3 (INEFFECTIVE LOWER FLANGE)

Specimen 17, 19, 20, 21, 61, and 98 fall in this group. Residual strengths range from 22 to 105 (in-kips), and a compliance of 8.00 (1000 in./in-kips) is typical of this group. Damage consists of a missing section of the lower flange or a through-cracked lower flange. Uniform reductions of 85 percent from values for nominally undamaged specimens is suggested for this group.

SECTION III

COMPARISONS OF MASS DISTRIBUTIONS AND TIME-INTEGRATION ALGORITHMS

Limited comparisons of the use of different mass distributions and time-integration schemes in CRAKD have been made. No difficulties have been encountered in the use of the Newmark- β method characterization of inertia; however, the diagonal mass matrix which results from a lumped-mass characterization allows efficient implementation of the central-difference integration scheme, since only trivial matrix inversion is required. In an attempt to shed some light on the relative accuracies and efficiencies of these methods, a problem, solved by Chen [2] using finite differences in space and time, has been the subject of numerical experiments.

Chen's problem consists of the plane-strain response of a centrally-cracked rectangular strip subjected to suddenly applied and maintained tension, σ , at each end. Properties of the strip were taken to correspond nominally to steel. The geometry of the problem is shown in Figure 12(a) where the shaded quadrant indicates the approximate mesh-point density (a total of 5000 points) employed by Chen in his finite-difference analysis. The stress-intensity factor was computed by multiplying components of stress by \sqrt{r} and fitting those near the crack-tip (data for two or three zones nearest the tip being discarded) to a straight-line spatial dependence on r . This straight line was then extrapolated to $r = 0$ to obtain K_I . Extrapolations along radial lines in several different directions were reported to agree within 5 percent. Chen's time-dependent stress-intensity factor normalized

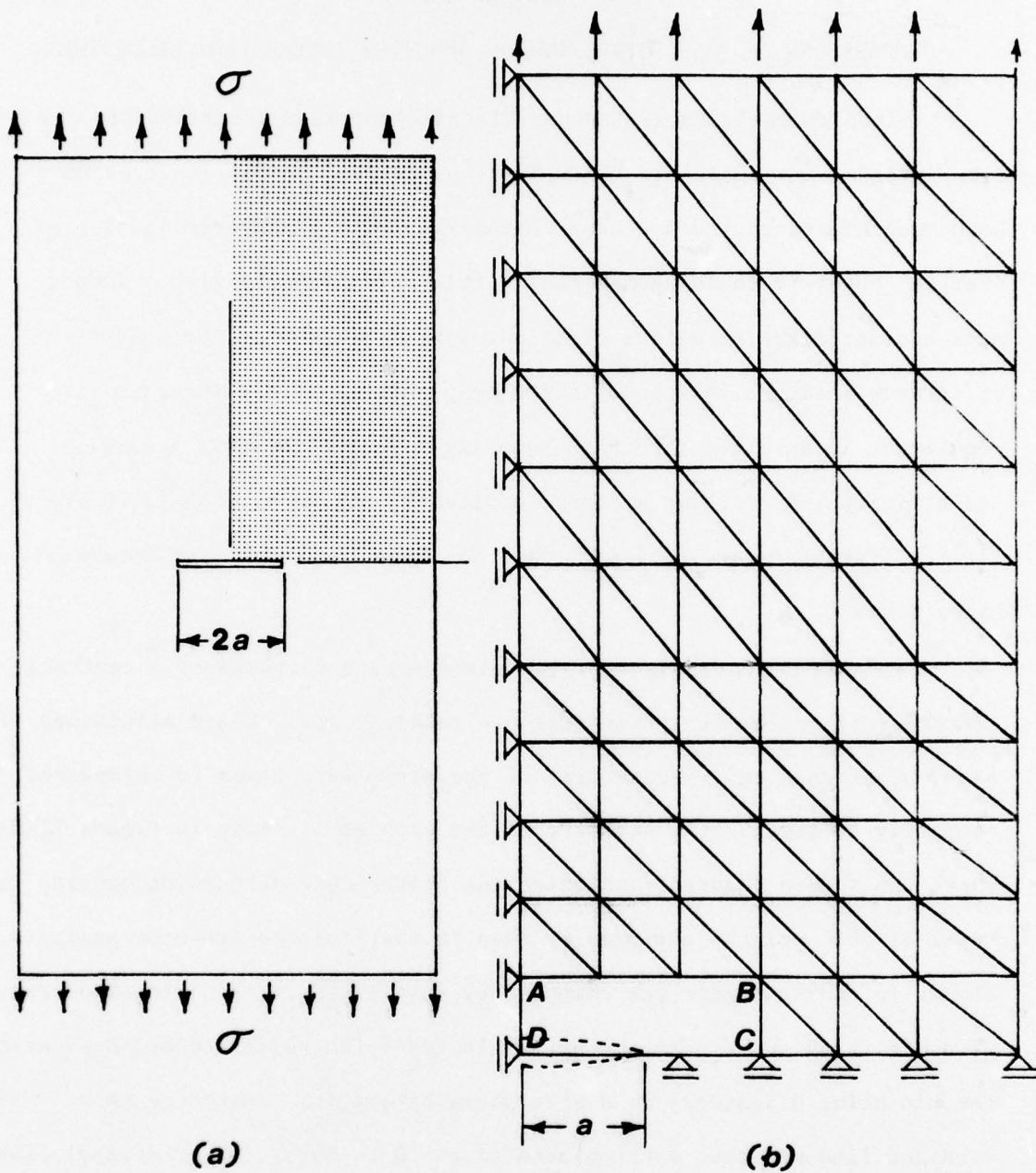


Figure 12. Chen's Problem and Its Finite-Element Representation

by $\sigma/\pi a$ is plotted in Figure 13. The symbols I, R, P, and S in Figure 13 were used by Chen to denote the time of arrival at the crack-tip of the longitudinal wave and the subsequent Rayleigh wave (from the other tip) and nearest-boundary reflections of pressure and shear waves, respectively. Subscripts 1 or 2 on these symbols indicate association with the first or second arrival of the longitudinal wave. The solid circles on Chen's curve mark values of K_I that correspond to the wave arrivals mentioned above.

A finite-element model representing the shaded quadrant of Chen's problem is shown in Figure 12(b). It consists of 84 nodes, 126 constant-strain triangles, and one 8-node singularity element ABCD. Depicted by open circles in Figure 13 are results obtained by this finite-element model using the consistent-mass characterization of inertia and the Newmark- β integration scheme. The time integration was accomplished with 75 steps each of 0.2 microsecond; this choice of time increment was motivated by the transit time (0.22 microsecond) of a longitudinal wave across the smallest of the triangular elements. The finite-element results, which are in substantial agreement with Chen's analysis, were obtained in 26 seconds of computation time on a UNIVAC 1108 computer during a low-demand period of the Georgia Institute of Technology time-sharing system.

With this analysis as a standard, some results of numerical experiments conducted on this finite-element model can now be considered. Firstly, time dependence of the stress-intensity factor predicted by a lumped-mass version of this model can be compared with that obtained from the consistent-mass version. This comparison is shown in Figure 14. In each case the Newmark- β method with a time step of 0.2 microsecond was employed. These results are

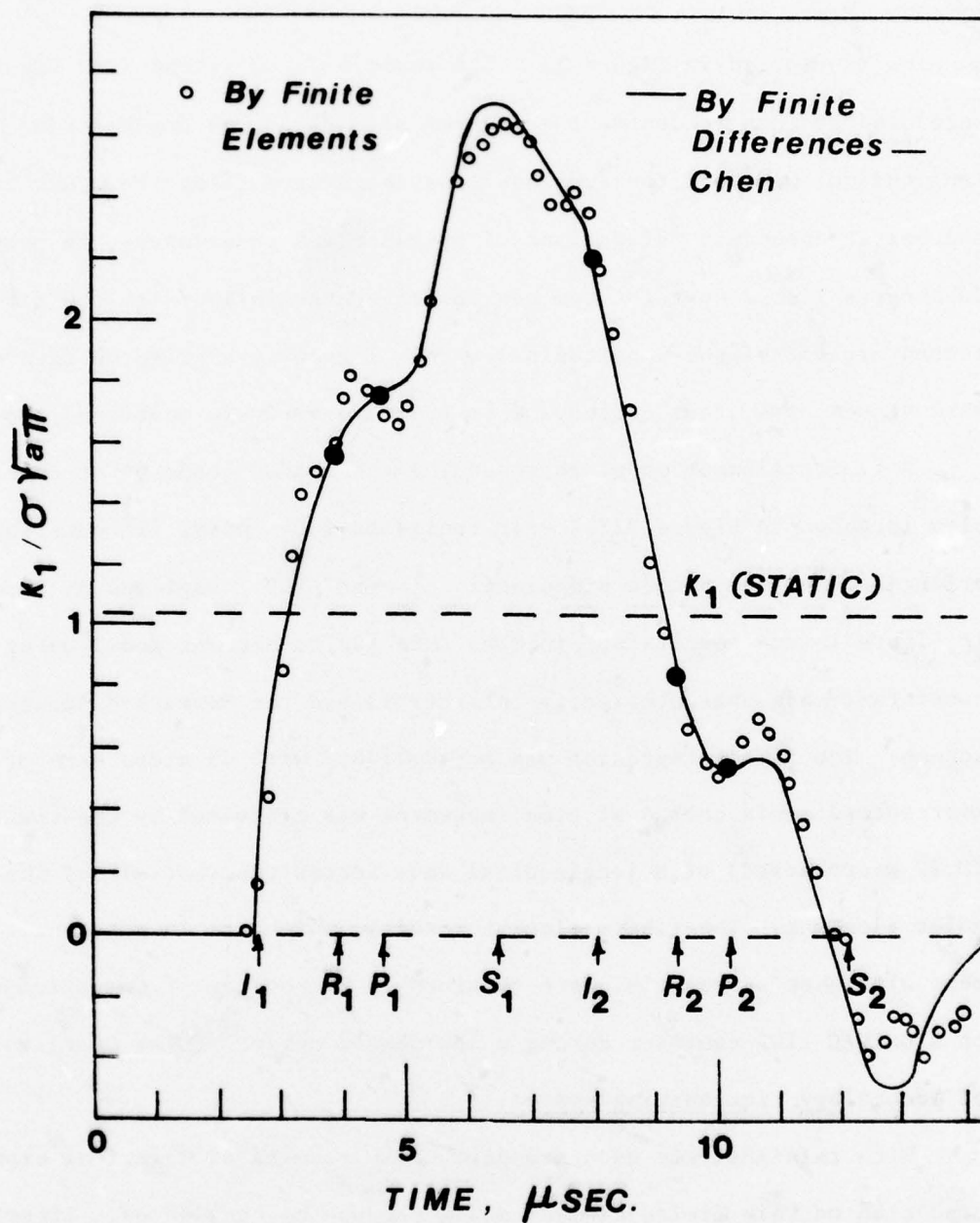


Figure 13. Comparison of Results Obtained Using Finite-Difference and Finite-Element Methods for Chen's Problem

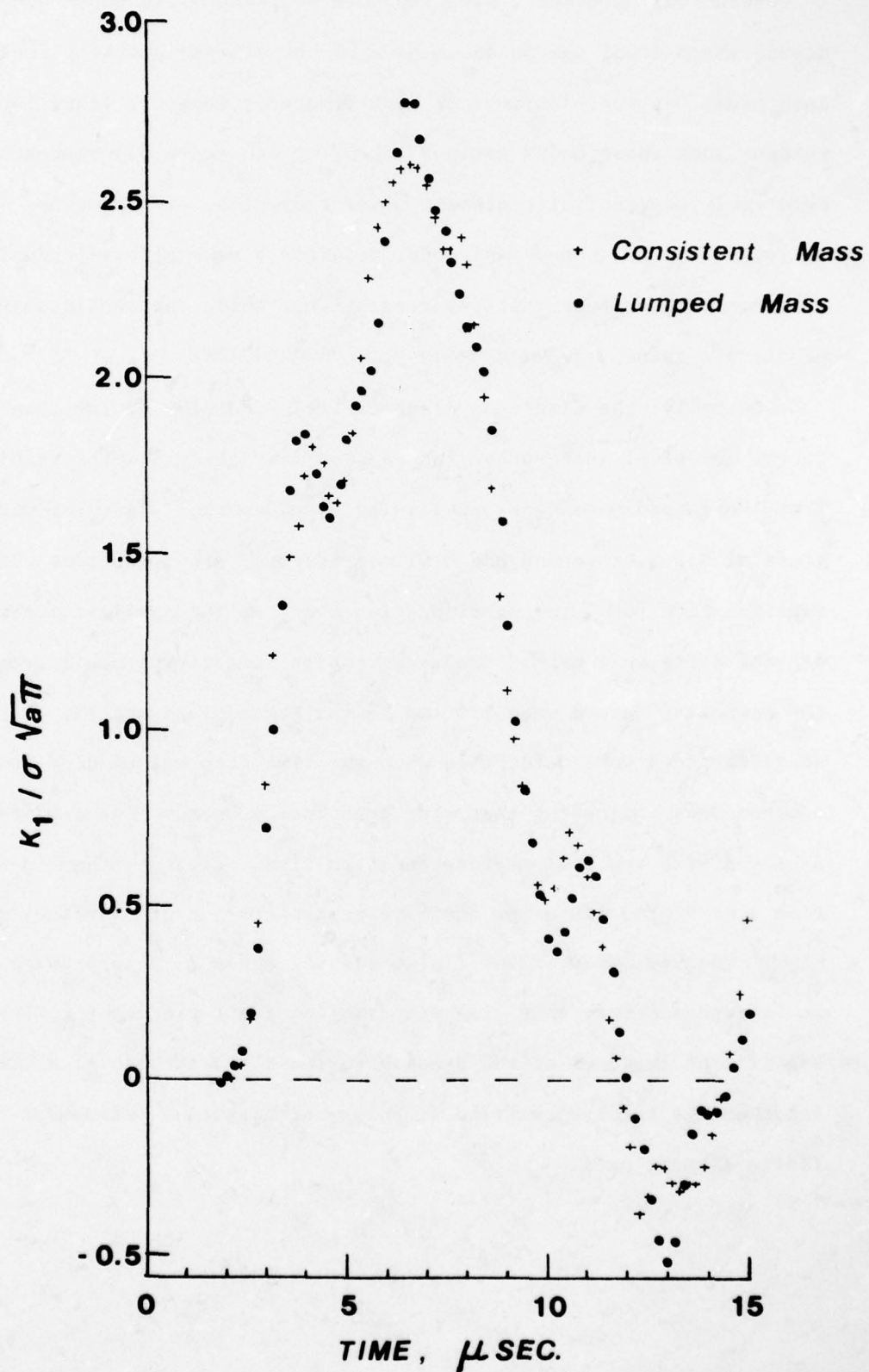


Figure 14. Effect of Inertia Characterization for Chen's Problem

in substantial agreement, with the most striking differences occurring around sharp local maxima and minima of the stress-intensity factor. At such times the contributions of high-frequency modes of vibration are most evident, and these modes are not likely to be accurately represented by the relatively coarse finite-element model regardless of the method of allocation of inertia. The lumped-mass model predicts a peak stress-intensity factor 5 percent higher than that reported by Chen while the consistent-mass model predicts a value 2 percent lower than that of Chen.

Secondly, the effect of a substantial reduction of the time step utilized in the numerical integration can be seen in Figure 15 where results obtained from the lumped-mass model, utilizing the Newmark- β algorithm with time steps of 0.2 microsecond and 0.01 microsecond, are presented. It can be remarked here for later consideration that, at the smaller time-step, the central difference method produces results indistinguishable from those of the Newmark- β method when plotted to the scale of Figure 15. Furthermore, no differences were detectable when the time step was reduced to 0.0027 microsecond, indicating that, for practical purposes, convergence has been achieved with the 0.01 microsecond step size. Clearly, the 0.2-microsecond time step is too large for accurate representation of contributions of the high-frequency modes of the finite-element model in this problem. However, it is apparent that this time step is adequate for characterizing the more significant features of the dynamic response and the use of a much smaller increment is hardly justified without a simultaneous refinement of the finite-element grid.

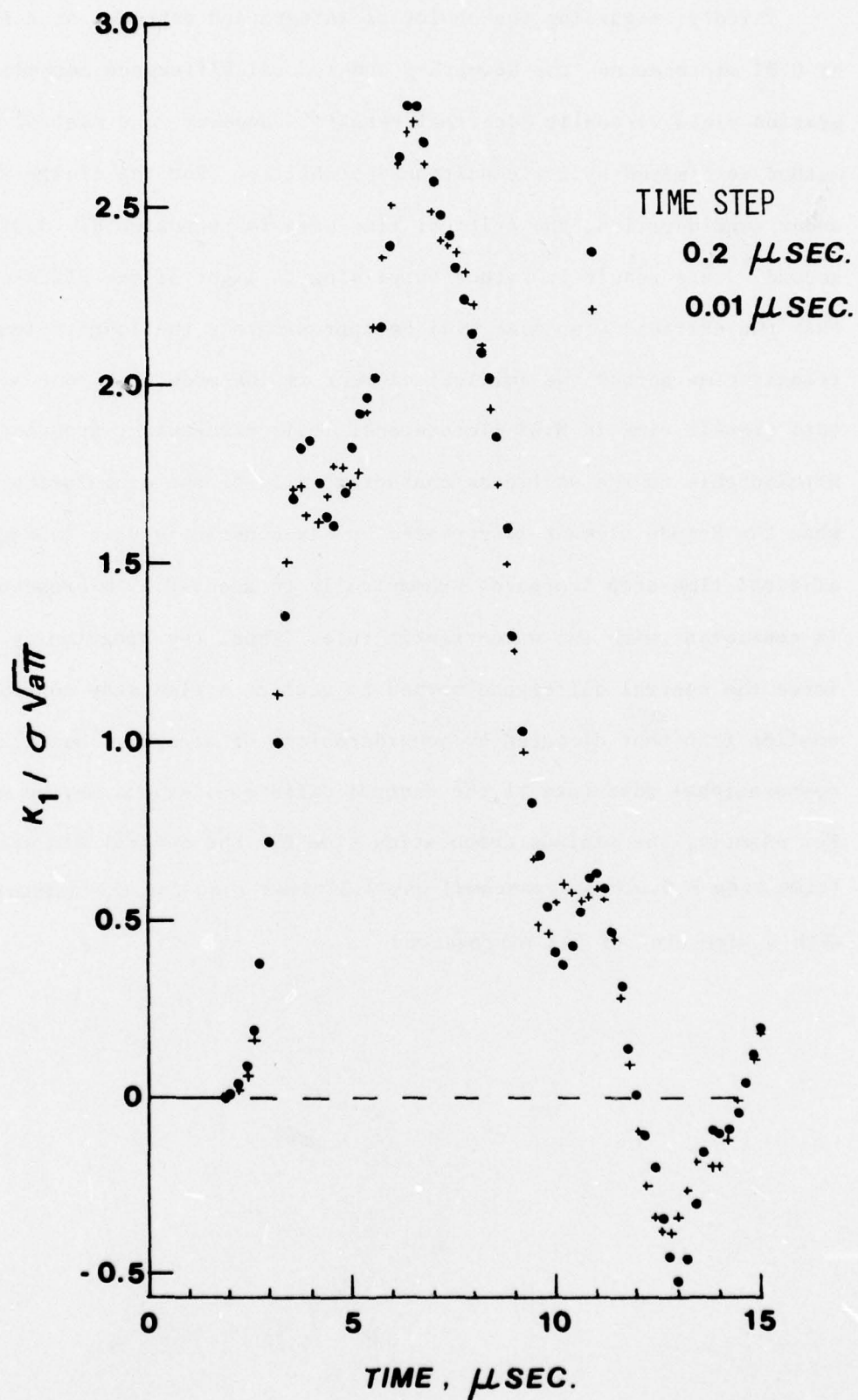


Figure 15. Effect of Time-Step Size for Chen's Problem

Thirdly, regarding the choice of integration schemes, at a time step of 0.01 microsecond the Newmark- β and central difference methods of integration yield virtually identical results. However, the central difference method is limited by its conditional stability. For the finite-element model under consideration, the critical time step is approximately 0.016 microsecond. This result is rather surprising in light of the often-used rule that the critical step size will be approximately the longitudinal-wave transit-time across the smallest element in the model; for our example, this transit time is 0.22 microsecond. This discrepancy apparently is attributable to the stiffness characteristics of the singularity element; when the 8-node element is replaced by six constant-strain triangles, the critical time step increases dramatically to about 0.19 microsecond which is consistent with the wave-transit rule. Thus, the singularity element may force the central difference method to utilize a time step considerably smaller than that dictated by considerations of accuracy; hence the intrinsic computational advantage of the central difference scheme may be negated. For example, the minimum computation time for the central difference method (time step = 0.016 microsecond) was 2.3 times that for the Newmark- β method with a time step of 0.2 microsecond.

SECTION IV

FINITE-ELEMENT SIMULATIONS OF IMPACT TESTS

4.1 INTRODUCTION

Impact of a falling weight with a precracked beam is an experimental method for determination of dynamic fracture toughnesses. Successful interpretation of such tests depends upon an accurate appraisal of the elastodynamics of both the specimen and the hammer; the ideal situation is one in which the hammer may be treated as a rigid body and the specimen behavior is quasi-static. However, often it is not possible to satisfy both of these conditions; in that event a dynamic finite-element analysis may play a useful role in predicting time-dependent stress-intensity factors. In this section are presented finite-element simulations of two such tests in which specimen inertia is significant.

4.2 THE TESTS OF MADISON AND IRWIN

In 1974 Madison and Irwin [3] published results of a fracture test program begun at Lehigh in 1966. The purpose of the program was to determine fracture toughness (K_{Ic}) values for structural steels at temperatures and loading rates representative of service conditions. The tests employed precracked three-point-bend specimens measuring 76mm deep, 300mm long and up to 25mm thick. The supported span was 250mm, and the fatigue crack length, including a starter notch, was approximately 25mm. Fracture toughness values were computed using the observed maximum load and the initial crack length adjusted to account for plastic-zone size. Loading times as brief as 0.50 ms were judged by Madison and Irwin to be "... small enough for evaluation of

minimum dynamic toughness and long enough to permit static stress analysis of the specimen." It is with this contention that the present work takes issue.

For a simply supported beam of flexural stiffness EI , mass M and span S , the fundamental frequency of vibration ω is given by

$$\omega = \pi^2 \sqrt{\frac{EI}{MS^3}} \quad (2)$$

For steel of dimensions appropriate to the test specimen, Equation (2) yields a fundamental period of about 0.37 ms--a figure much too near the least loading period to warrant neglecting inertia effects. This elementary calculation neglects shear deformation and rotary inertia, beam overhang, and the presence of the crack. But since these are all effects tending to increase the computed fundamental period, a static analysis seems all the more suspect.

In the Madison-Irwin experiments, the specimen was loaded by an instrumented striking tup mounted in a freely falling weight. The instrumentation provided an oscilloscope trace of the applied load. Two-peak load histories were reported for some of the tests, which Madison and Irwin attributed to obscuring inertia effects. They associated the first peak with inertia effects, while the second peak was judged to be the significant specimen-load record. By placing loading cushions between the specimen and the striking tup, Madison and Irwin obtained a load record with a single peak. This was accepted as evidence that inertia effects had been eliminated, and they supposed in their calculations that the peak recorded load was the specimen

load at the onset of crack propagation. Figure 16 shows a best-estimate reproduction of a published oscilloscope trace recorded in a -40°C test of a 25mm-thick specimen. The load history depicted in Figure 16 is the type deemed acceptable by Madison and Irwin for static analysis of the problem.

Madison and Irwin used a slightly modified Gross-Srawley formula in conjunction with the peak load from the specimen-load record to obtain a first-estimate value of K_c . Their formula,

$$K = \frac{3PS/a}{2BW^2} \left[1.93 - 3.12 \frac{a}{w} + 14.7 \left(\frac{a}{w} \right)^2 - 25.3 \left(\frac{a}{w} \right)^3 + 25.9 \left(\frac{a}{w} \right)^4 \right], \quad (3)$$

gives K in $\text{MPa}\sqrt{\text{m}}$ for P in MN with beam span S , thickness B , depth W and crack length a all in m. For the peak load (55.6 kN) obtained from Figure 16, Equation (3) yields a first-estimate K_c of $43.7 \text{ MPa}\sqrt{\text{m}}$.

Such figures were subsequently revised upward by adjusting for plastic-zone size. Briefly this amounted to increasing the fatigue crack length by the plastic-zone radius

$$r_Y = \frac{1}{\sigma_Y} \left(\frac{K}{\sigma_Y} \right)^2, \quad (4)$$

in which σ_Y is the yield stress. Equations (3) and (4) were then used repeatedly until the iteration scheme produced practically constant values for r_Y and K_c . Since the thrust of the present work has to do with assessing inertia effects rather than plasticity effects, no plasticity adjustments will be made to either these results or those of Madison and Irwin.

Figure 17 shows a finite-element representation of a Madison-Irwin test specimen. Due to symmetry about the plane of the crack, only the left half of the specimen is modelled. The model consists of 163 nodes, 273 constant-

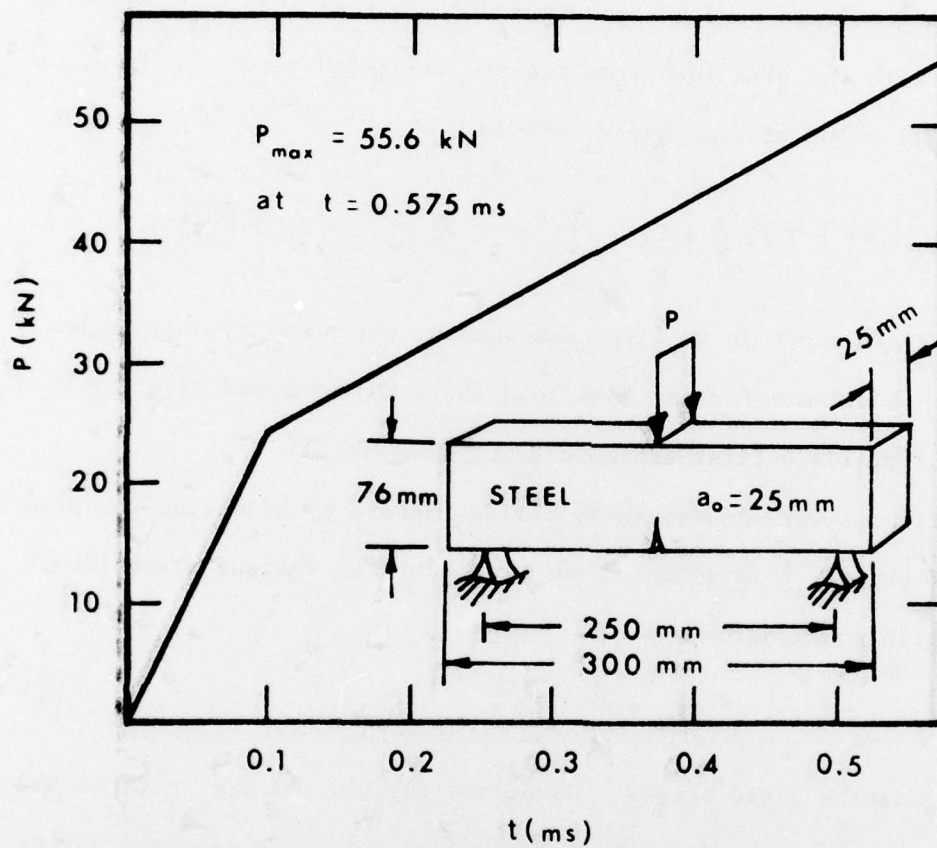


Figure 16. Geometry and Load-Record in the Madison-Irwin Impact Test

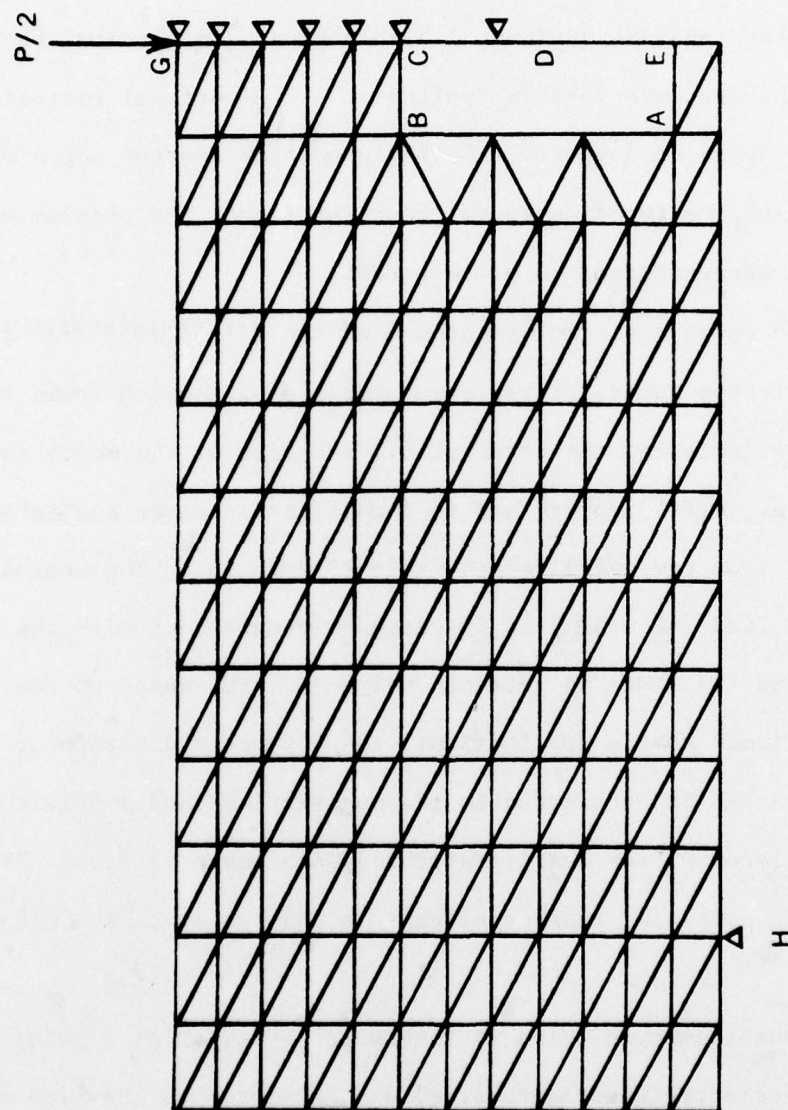


Figure 17. Finite-Element Model of the Madison-Irwin Specimen

strain triangles, and 1 eight-node crack-tip singularity element. The singularity element ABCDE is required to accurately represent the locally severe stress gradients in the neighborhood of the fatigue crack tip at D. Consistent with symmetry requirements, nodes along the crack's prolongation DG are restrained against horizontal displacement. A vertical force equal to one-half the specimen load is applied at G. A vertical restraint at H simulates the specimen support. The fatigue-crack starter notch was not represented, and the two-dimensional idealization of the problem was taken to be the one corresponding to plane stress.

Figure 18 shows the time dependence of the stress-intensity factor K_I for three different numerical representations of a Madison-Irwin experiment. The solid line indicates the quasi-static response of the model shown in Figure 18, i.e., $K_I(t)$ appropriate to a massless specimen subjected to the load as taken from the oscilloscope trace (Figure 16). The computed value of K_I at peak load ($42 \text{ MPa}\sqrt{\text{m}}$) is in reasonable agreement with the Madison-Irwin estimates ($43.7 \text{ MPa}\sqrt{\text{m}}$) obtained using (3), but based on the results of previous confirmed static applications, the 4 percent discrepancy is somewhat more than can be attributed to the numerical method. Notwithstanding the small difference, the quasi-static response shown in Figure 18 is used as a basis for assessing inertia effects in the two companion dynamic executions.

The locus of empty circles in Figure 18 is $K_I(t)$ for a model with inertia characteristics corresponding to steel and subjected to the time-dependent load of Figure 16. The integration time step was 10^{-2} ms , and K_I was computed at each time step. The smoothness and shape of the response indicates the

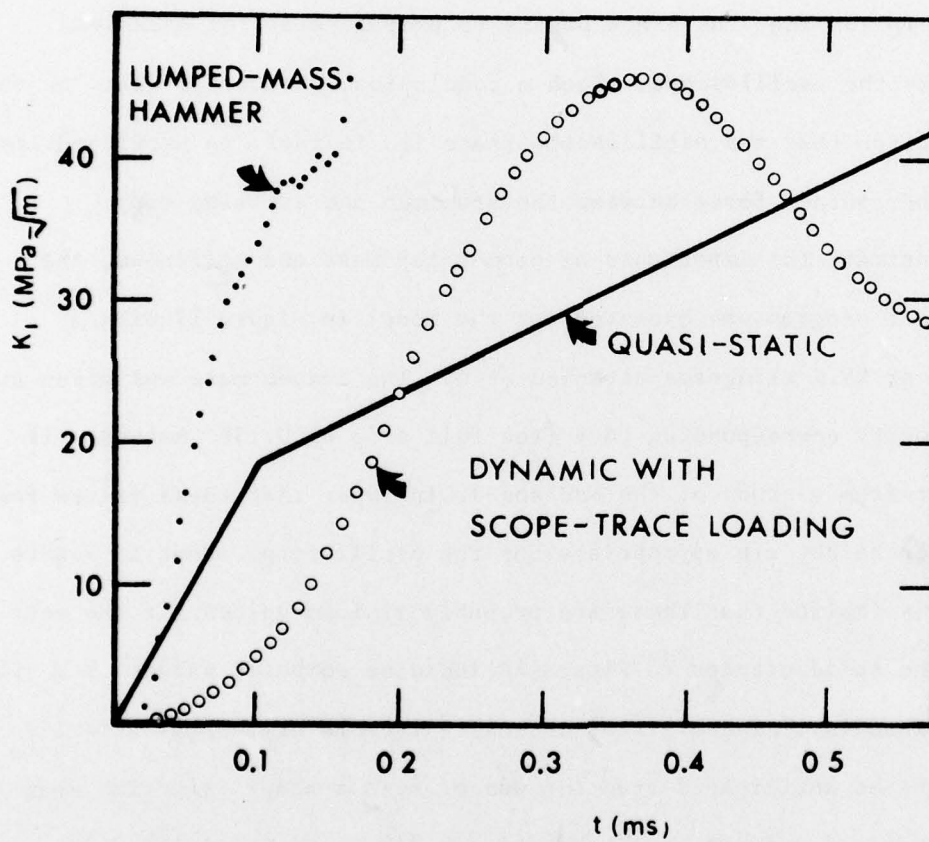


Figure 18. Results of Finite-Element Analyses of the Madison-Irwin Impact Test

adequacy of this time step and confirms the earlier estimate of the period. The considerable difference between the dynamic and quasi-static responses is exclusively the result of specimen inertia. When specimen inertia is included, the peak stress-intensity factor is elevated by more than 8 percent above the maximum quasi-static value. More importantly, the peaks occur at significantly different times. So for the particular geometry and loading rate under consideration, the dynamic result is in clear conflict with an assumption that the crack begins to propagate at the peak load registered by the oscilloscope. Such a conclusion, of course, rests on the tacit assumption that the oscilloscope trace is, in fact, an accurate time record of the contact force between the specimen and striking tup.

To illustrate the importance of hammer-tup mass and stiffness, the finite-element program was executed for the model in Figure 17 with a lumped-mass of 45.4 kilograms attached at G. The lumped-mass was given an initial velocity corresponding to a free-fall drop of 0.152 meters. It is not clear from a study of the Madison-Irwin paper that these values for mass and drop height are appropriate for the oscilloscope trace in Figure 16, but it is implied that these are probably minimum values for the test program. The solid circles in Figure 18 indicate computed values of K_I for this representation. These stress-intensity factors are unrealistically high as might be anticipated from the use of such a model in a time span in which non-rigid motions of the hammer are likely to be significant.

No claim is made to a successful prediction of time-dependent stress-intensity factors for the impact test that has been discussed. Rather, the analyses which have been presented call attention to the danger of ignoring

specimen inertia or of an oversimplified model of the hammer. It is the writer's opinion that for relatively high-velocity impact, involving a hammer and specimen of similar materials, an analytical model which accounts for the elastodynamics of the specimen and at least that portion of the hammer tup between the specimen and the load transducer is required.

4.3 THE TESTS OF KOBAYASHI AND CHAN

Depicted in Figure 19 is a finite-element model of a dynamic-tear-test specimen of Homalite-100, a photoelastic material, with which experiments have been conducted by Kobayashi and Chan [4]. The specimen support and loading configuration is the same as that of the preceding section except for specimen dimensions and hammer mass. Since steel has an acoustic impedance of approximately eighteen times that of Homalite-100 and a longitudinal-wave speed of about two and one-half that of Homalite-100, it is reasonable to regard the hammer as a rigid body in an analysis of the specimen. Thus, as indicated in Figure 19, which depicts only one-half of the specimen because of symmetry, the node corresponding to the impact point is assigned a mass equal to one-half the mass, $M = 1.47$ kg, of the hammer. This node is then given an initial velocity, $v_0 = 1.58$ m/s, equal to the impact velocity; all other nodes have zero initial velocity.

Since the specimen is relatively thin (0.0095 meter), plane-stress forms of the elements were used in the computations which were carried out using the consistent-mass Newmark- β scheme (time step = 2 microseconds) for a crack length of 0.005 meter. The numerical results are given in Figure 20 where the stress-intensity factor and hammer acceleration are plotted for the

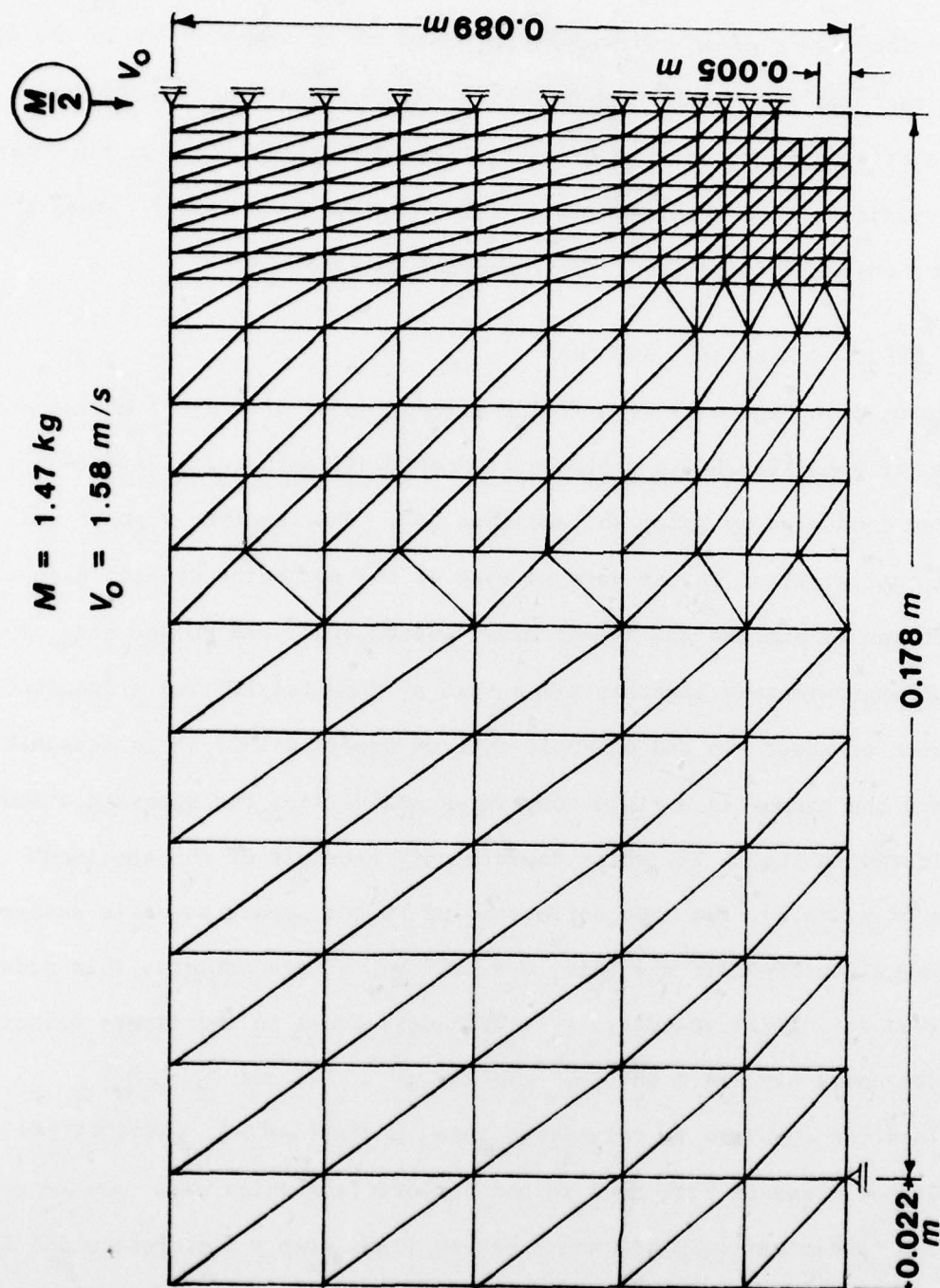


Figure 19. Finite-Element Model of the Kobayashi-Chan Dynamic Tear Test

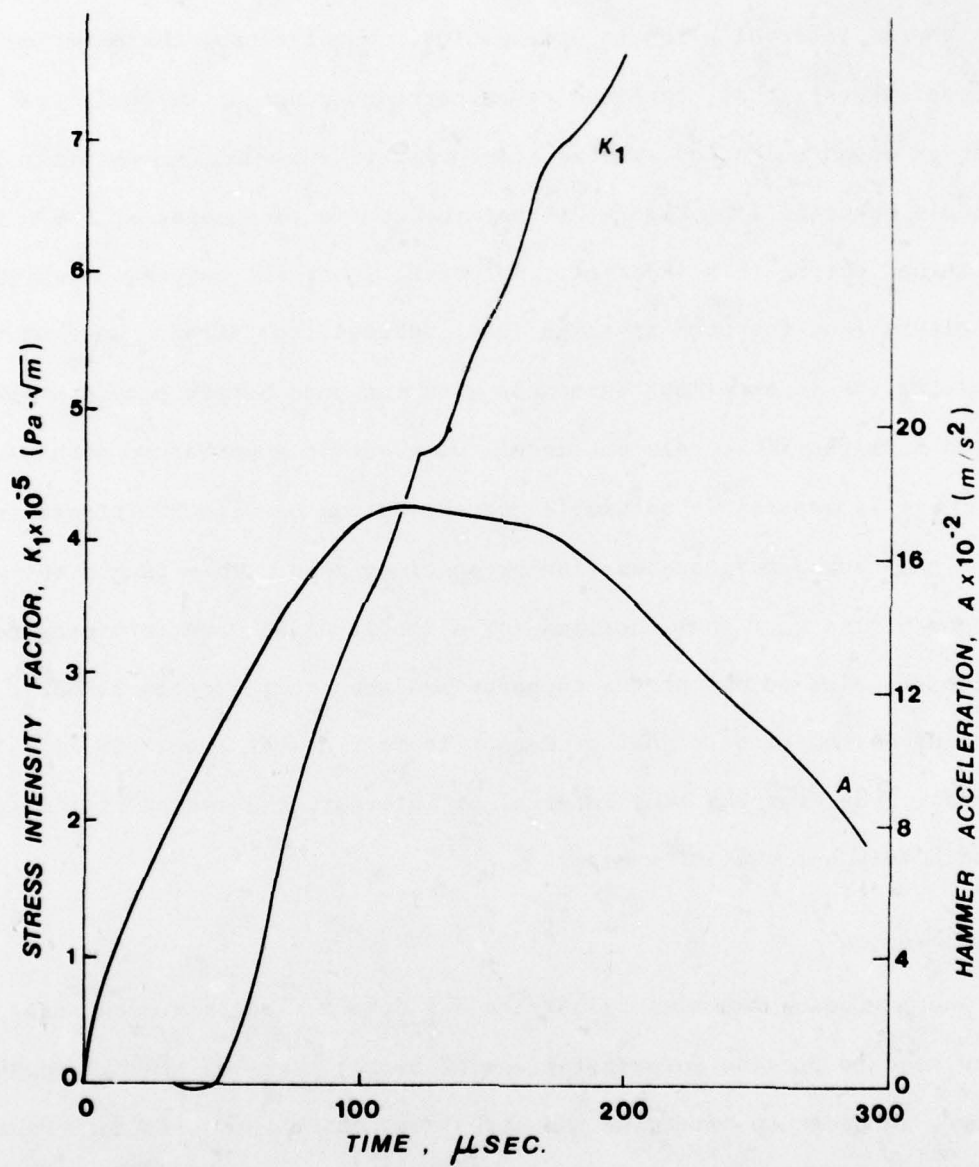


Figure 20. Computed K_I and Hammer Acceleration for a Dynamic Tear Test

first 200 microseconds following contact of the hammer with the specimen. The Kobayashi-Chan experiments were concerned primarily with the crack propagation phase of the motion, and they reported only limited data that bears on the interval prior to propagation. Nonetheless, the experimental evidence suggests that, for conditions corresponding to the analytical model, the crack began to extend at some time prior to 200 microseconds after impact. It should be noted from Figure 20 that the static toughness, $K_c = 606 \text{ kPa}\sqrt{\text{m}}$, is attained during this interval. Moreover, Kobayashi has communicated to the writers that the peak specimen load, deduced from strain gages on the hammer tup, is in excellent agreement with the peak hammer acceleration deduced from the finite-element model. Of greatest importance, perhaps, is that there is apparently no simple correspondence between the stress-intensity factor and the hammer acceleration or specimen load. This is not surprising in light of the fact that the time for a longitudinal wave to propagate from the impact point to one of the supports and then to the crack is about 185 microseconds (the first signal of impact is felt at the crack tip at 44 microseconds). Thus, for the time interval of interest, the motion of the specimen is definitely not that of a beam.

5.4 CONCLUSION

The preceding examples illustrate how dynamic finite-element analyses may be used to provide interpretations of impact tests on precracked specimens. However, in order to determine the stress-intensity factor at the onset of crack propagation, it is necessary to ascertain from experimental measurements a close estimate of the time at which propagation commences. Moreover, the load-time record at the impact site must be determined unless the behavior of the impacting hammer can be described by a reasonably simple analytical model.

SECTION V

CONCLUSIONS

Condition of the lower (tension) flange proved to be the primary determinant of residual strength of the damaged specimens. An ineffective lower flange (either due to a through crack or missing section) can lead to a reduction in strength of more than 85 percent. Gouges in the tip of the lower flange that involve its full 5/8-inch thickness and are at least 1/4-inch deep provide a 40-percent reduction in strength and stiffness.

Linear elastic fracture mechanics may be used to more tightly define reductions in strength when there are visible cracks in the beam. Damage sites do not effectively reinforce one another unless they are practically contiguous. Gouges or even holes in the web are of little detriment to strength. An unsupported length of 18 inches will buckle in a torsional mode at a bending moment of about 600 in-kips.

With regard to the finite-element analyses of elastodynamic problems, the following conclusions are offered:

1. No evidence has been obtained to suggest a clear advantage for either of the mass distributions (lumped or consistent).
2. The computational advantage of the central-difference method is negated by the extremely small time step required for numerical stability when crack tip singularity elements are employed.
3. The finite-element method presented in this report can be a useful tool in interpreting the results of impact tests on precracked specimens.

REFERENCES

1. Chan, S. P., Cox, H. L. and Benfield, W. A., Transient Analysis of Forced Vibration of Complex Structural-Mechanical Systems. Journal of the Royal Aeronautical Society, Volume 66, 1962, pp. 457-460.
2. Chen, Y. M., Numerical Computation of Dynamic Stress Intensity Factors by a Lagrangian Finite-Difference Method (the Hemp Code). Engineering Fracture Mechanics, Volume 7, 1975, pp. 653-660.
3. Madison, R. B. and Irwin, G. R., Dynamic K_c Testing of Structural Steel. Journal of the Structural Division, ASCE, Volume 100, No. ST7, 1974, pp. 1331-1349.
4. Kobayashi, A. S. and Chan, C. F., A Dynamic Photoelastic Analysis of Dynamic-tear-test-specimen. Experimental Mechanics, Volume 16, No. 5, 1976, pp. 176-181.

INITIAL DISTRIBUTION

Hq USAF/SAMI	1
Hq USAFE/DOQ	1
Hq PACAF/DOOFQ	3
Hq TAC/DRA	1
ASD/ENFEA	2
AUL/LSE 71-249	1
OO/ALC/MMWMP	2
AFIS/INT	1
DDC-TC	2
AFATL/DLODL	2
AFATL/DL	1
AFATL/DLD	1
AFATL/DLY	1
ASD/XRP	1
US Army TRADOC Sys Ana Act/ ATAA-SL	1
COMIPAC/I-232	1
School of Engineering Science and Mechanics/Georgia Inst of Tech	15
Off of Engineering Research/ Oklahoma State University	1
AMSAA/DRXSJ-J	1
Inst of Fracture and Solid Mech/ Lehigh University	1
Systems, Science and Software	1
AFFDL/FBR	1
AFFDL/FBR(ASIAC)	1
NSWC/DL	1
PACMISTESTCEN/Code 1245	1
BRL-BLV	1
NWC/Code 3261	1
Dept of Engineering Sciences/ University of Florida	1
Univ of Florida Grad Center	1
AFATL/DLYV	10
TAC/INAT	1
AFFDL/FES	1
NWC/Code 318	2